A Novel Framework for Molecular Characterization of Atmospheric Organic Aerosol Based on Collision Cross Section and Mass-to-Charge Ratio

X. Zhang[1], J. E. Krechmer[2,3], M. Groessl[4], W. Xu[1], S. Graf[4], M. Cubison[4],

J. T. Jayne[1], J.L. Jimenez[2,3], D. R. Worsnop[1], and M. R. Canagaratna[1]

[1] Center for Aerosol and Cloud Chemistry, Aerodyne Research Inc., Billerica, MA 01821, USA

[2] Department of Chemistry and Biochemistry, University of Colorado, Boulder, CO 80309, USA

[3] Cooperative Institute for Research in Environmental Sciences, Boulder, CO 80309, USA

[4] TOFWERK, CH-3600 Thun, Switzerland

Correspondence to: M. R. Canagaratna (mrcana@aerodyne.com)

Atmospheric
Chemistry
and Physics
Discussions

Open Access

EGU

1 **Abstract**

2   A new metric is introduced for representing the molecular signature of atmospheric

3   organic aerosols, the collision cross section (Ω), a quantity that is related to the structure

4   and geometry of molecules and is derived from ion mobility measurements. By

5   combination with the mass-to-charge ratio (*m/z*), a two-dimensional $\Omega - m/z$ space is

6   developed to facilitate the comprehensive investigation of the complex organic aerosol

7   mixture. A unique distribution pattern of chemical classes, characterized by functional

8   groups including amine, alcohol, carbonyl, carboxylic acid, ester, and organic sulfate, is

9   developed on the 2-D $\Omega - m/z$ space. Species of the same chemical class, despite

10   variations in the molecular structures, tend to situate as a narrow band on the space and

11   follow a trend line. Reactions involving changes in functionalization and fragmentation

12   can be represented by the directionalities along or across these trend lines, thus allowing

13   for the interpretation of mechanisms associated with the formation and evolution of

14   atmospheric organic aerosol. The characteristics of trend lines for a variety of

15   functionalities that are commonly present in ambient aerosols can be predicted by the

16   core model simulations, which provide a useful tool to identify the chemical class to

17   which an unknown species belongs on the $\Omega - m/z$ space. Within the band produced by

18   each chemical class on the space, molecular structural assignment can be achieved by

19   utilizing collision induced dissociation as well as by comparing the measured collision

20   cross sections in the context of those obtained via molecular dynamics simulations.

21

22

23

24

25

26

27

Atmospheric
Chemistry
and Physics
Discussions

1. Introduction

28

29   Organic aerosol (OA) constitutes a major fraction of sub-micrometer atmospheric

30   particulate matter and comprises a complex and dynamic system linking source emission,

31   chemical transformation, and phase partitioning (Hallquist et al., 2009). It consists of a

32   multitude of organic species that arise from primary emissions and secondary

33   productions. Once in the atmosphere, OA species actively evolve via gas-particle

34   conversion and multiphase chemistry. The complexity and dynamic behaviors of ambient

35   OA have rendered identification of major pathways contributing to OA budget difficult

36   and have limited our capability to evaluate its impact on human health and global

37   climate.

38   Several two-dimensional frameworks have been developed in an effort to deconvolve

39   the complexity of OA mixtures and visualize their atmospheric transformations. The Van

40   Krevelen diagram, which scatter plots the hydrogen-to-carbon atomic ratio (H:C) and the

41   oxygen-to-carbon atomic ratio (O:C), has been widely used to represent the bulk

42   elemental composition and the degree of oxygenation of organic aerosol (Heald et al.,

43   2010). The average carbon oxidation state ($\overline{OS}_C$), a quantity that necessarily increases

44   upon oxidation, can be estimated from the elemental ratios (Kroll et al., 2011). When

45   coupled with carbon number (n_C), it provides constraints on the chemical composition of

46   organic aerosol and defines key classes of atmospheric processes based on the unique

47   trajectory of the evolving OA composition on the $\overline{OS}_C - n_C$ space. The degree of

48   oxidation has also been combined with the volatility (expressed as the effective saturation

49   concentration, C^*), forming a 2-D volatility basis set to describe the coupled aging and

50   phase partitioning of organic aerosol (Donahue et al., 2012). These three spaces are

51   designed to represent fundamental properties of the OA mixture and provide insight into

52   the OA chemical evolution in the atmosphere. Organic aerosol components span large

53   varieties in the physicochemical properties. Species of similar volatility or elemental

54   composition can differ vastly in structures and functionalities. One weakness of these

55   frameworks is that they do not provide information on the OA components at molecular

56   level.

Atmospheric
Chemistry
and Physics
Discussions

57   In this article we introduce a new framework that is based on the collision cross

58   section (Ω), a quantity that is related to the structure and geometry of a molecule. The

59   collision cross section of a charged molecule determines its mobility as it travels through

60   a neutral buffer gas such as N_2 under the influence of a weak and uniform electric field.

61   Species with open conformation undergo more collisions with buffer gas molecules and

62   hence travel more slowly than the compact ones (Shvartsburg et al., 2000; Eiceman et al.,

63   2013). Mobility measurements are usually performed with an Ion Mobility Spectrometer

64   (IMS), where ions are separated mainly on the basis of their size, geometry, as well as

65   interactions with the buffer gas. The combination of IMS with a Mass Spectrometer (MS)

66   allows for further selection of ions based on their mass-to-charge ratios. The resulting

67   IMS-MS plot provides separation of molecules according to two different properties:

68   geometry (as reflected by the collision cross section) and mass (as reflected by the mass-

69   to-charge ratio) (Kanu et al., 2008). The Ion Mobility Spectrometry - Mass Spectrometry

70   (IMS-MS) analytical technique has been widely employed in the fields of biochemistry

71   (McLean et al., 2005; Liu et al., 2007; Dwivedi et al., 2008; Roscioli et al., 2013; Groessl

72   et al., 2015) and homeland security (Eiceman and Stone, 2004; Ewing et al., 2001;

73   Fernandez-Maestre et al., 2010). To our knowledge, the application of IMS-MS to study

74   organic species in the atmosphere, however, has only been explored very recently

75   (Krechmer et al., 2016).

76   We propose a two-dimensional collision cross section vs. mass-to-charge ratio ($\Omega -$

77   m/z) space to facilitate the comprehensive investigation of complex OA mixtures. Despite

78   the typical complexity of the detailed molecular mechanism of OA production and

79   evolution, oxidized molecules that constitute OA can be characterized by their distinctive

80   functional groups (Zhang and Seinfeld, 2013). We show that the investigated organic

81   classes ($m/z < 600$), characterized by functional groups including amine, alcohol,

82   carbonyl, carboxylic acid, ester, and organic sulfate, exhibit unique distribution patterns

83   on the $\Omega - m/z$ space. Species of the same chemical class, despite variations in the

84   molecular structures, tend to develop a narrow band and follow a trend line on the space.

85   Reactions involving changes in functionalization and fragmentation can be represented

86   by directionalities along or across these trend lines. The locations and slopes of the

87   measured trend lines are shown to be predicted by the core model (Mason et al., 1972),

4

Atmospheric
Chemistry
and Physics
Discussions

88   which characterizes the ion-neutral interactions as elastic sphere collisions. Within the

89   narrow band produced by each chemical class on the $\Omega - m/z$ space, molecular structural

90   assignment is achieved with the assistance of collision induced dissociation analysis.

91   Measured collision cross sections are also shown to be consistent with theoretically

92   predicted values from the trajectory method (Mesleh et al., 1996; Shvartsburg and

93   Jarrold, 1996) and are used to identify isomers that are separated from an isomeric

94   mixture.

95

96   **2. Collision Cross Section Measurements**

97   2.1 Materials

98   A collection of chemical standards (ACS grade, $\geq$ 96%, purchased from Sigma

99   Aldrich, St. Louis, MO, USA), classified as amines, alcohols, carbonyls, carboxylic

100 acids, esters, phenols, and organic sulfates, were used to characterize the performance of

101 IMS-MS. These chemicals were dissolved in an HPLC-grade solvent consisting of a 70%

102 methanol / 29% water with 1% formic acid, at a concentration of approximately 10 µM.

103 2.2 Instrumentation

104 Ion mobility measurements were performed using an Electrospray Ionization (ESI)

105 Drift-Tube Ion Mobility Spectrometer (DT-IMS) interfaced to a Time-of-Flight Mass

106 Spectrometer (TOFMS). The instrument was designed and manufactured by TOFWERK

107 (Switzerland), with detailed descriptions and schematics provided by several recent

108 studies (Kaplan et al., 2010; Zhang et al., 2014; Groessl et al., 2015; Krechmer et al.,

109 2016). In the next few paragraphs, we will present the operating conditions of the ESI-

110 IMS-TOFMS instrument.

111 Solutions of chemical standards were delivered to the ESI source via a 250 µL gas-

112 tight syringe (Hamilton, Reno, NV, USA) held on a syringe pump (Harvard Apparatus,

113 Holliston, MA, USA) at a flow rate of 1 µL min⁻¹. A deactivated fused silica capillary

114 (360 µm OD, 50 µm ID, 50 cm length, New Objective, Woburn, MA, USA) was used as

115 the sample transfer line. The ESI source was equipped with an uncoated SilicaTip Emitter

116 (360 µm OD, 50 µm ID, 30 µm tip ID, New Objective, Woburn, MA, USA) and

Atmospheric
Chemistry
and Physics
Discussions

117 connected to the capillary through a conductive micro union (IDEX Health & Science,

118 Oak Harbor, WA, USA). The ESI emitter was operated at both positive and negative

119 mode at a capillary voltage of $\pm (1.5 - 2.0)$ kV. The charged droplets generated at the

120 emitter tip migrate through a desolvation region in nitrogen atmosphere at room

121 temperature, where ions evaporate from the droplets and are introduced into the drift tube

122 through a Bradbury-Nielsen ion gate located at the entrance. The ion gate was operated in

123 the Hadamard Transform mode, with a closure voltage of ± 50 V and an average gate

124 pulse frequency of 1.2×10^3 Hz. The drift tube was held at a constant temperature (340 ± 3

125 K) and atmospheric pressure (~ 1019 *mbar*). A counter flow of N_2 drift gas was

126 introduced at the end of the drift region at a flow rate of 1.2 L min^{-1}. Ion mobility

127 separation was carried out at a typical filed strength of $300 - 400$ V cm^{-1}, resulting in a

128 reduced electric field of approximately $1.4 - 1.8$ Td. After exiting from the drift tube,

129 ions were focused into TOFMS through a pressure-vacuum interface that includes two

130 segmented quadrupoles that were operated at ~ 2 *mbar* and $\sim 5 \times 10^{-3}$ *mbar*, respectively.

131 Collision Induced Dissociation (CID) of parent ions is achieved by adjusting the voltages

132 on the ion optical elements between the two quadruple stages (Kaplan et al., 2010).

133   The ESI-IMS-TOFMS instrument was operated in the *m/z* range of 40 to 1500 with a

134 total recording time of 90 s for each dataset. The Mass Spectrometer was calibrated using

135 a mixture of quaternary ammonium salts, reserpine, and a mixture of fluorinated

136 phosphazines (Ultramark 1621) in the positive mode and ammonium phosphate, sodium

137 dodecyl sulfate, sodium taurocholate hydrate, and Ultramark 1621 in the negative mode.

138 The ion mobility measurements were calibrated using tetraethyl ammonium chloride as

139 the instrument standard and 2,4-lutidine as the mobility standard, as defined shortly

140 (Fernández-Maestre et al., 2010). Mass spectra and ion mobility spectra were recorded

141 using the acquisition package "Acquility" (v2.1.0, http://www.tofwerk.com/acquility).

142 Post-processing was performed using the data analysis package "Tofware" (version 2.5.3,

143 www.tofwerk.com/tofware) running in the Igor Pro (Wavemetrics, OR, USA)

144 environment.

Atmospheric
Chemistry
and Physics
Discussions

145   2.3 Calculations

146   The average velocity of an ion in the drift tube (v_d) is proportional to its characteristic

147   mobility constant (K / cm^2 V^{-1} s^{-1}) and the electric field intensity (E_d), provided that the

148   field is weak (McDaniel and Mason, 1973):

149     $$v_d = K\,E_d \tag{1}$$

150   Experimentally, ion mobility constants can be approximated from the time of ion clouds

151   spent in the drift tube (t_d / s), given by the rearranged form of Equation (1):

152     $$t_d = \frac{1}{K}\,\frac{L_d^2}{V_d} \tag{2}$$

153   where L_d (cm) is the length of the drift tube and V_d (V) is the drift voltage. In the present

154   study, drift time measurements were carried out at six different drift voltages ranging

155   from 5 kV to 8 kV in ~ 1019 $mbar$ of nitrogen gas at 340 K (Figure S1 in the

156   supplement). The ion mobility constant (K) is derived by linear regression of the recorded

157   arrival time (t_a) of the ion clouds at the detector versus the reciprocal drift voltage:

158     $$t_a = \frac{L_d^2}{K}\,\frac{1}{V_d} + t_0 \tag{3}$$

159   Note that the arrival time was determined from the centroid of the best-fit Gaussian

160   distribution, see Figure S2 in the Supplement. The y-intercept of the best-fit line

161   represents the transport time of the ion from the exit of the drift tube to the MS detector

162   (t_0), which exhibits strong m/z dependency that is attributable to a time-of-flight

163   separation in the ion optics, see Figure S3 in the Supplement.

164   It is practical to discuss an ion's mobility in terms of the reduced mobility constant

165   (K_0), defined as:

166     $$K_0 = K\,\frac{273.15}{T}\,\frac{P}{1013.25} \tag{4}$$

167   where P ($mbar$) is the pressure in the drift region and T (K) is the buffer gas temperature.

168   In theory, the parameter K_0 is constant for a given ion in a given buffer gas and can be

169   used to characterize the intrinsic interactions of that particular ion-molecule pair. In

170   practice, however, K_0 values from different measurements might not be in good

Atmospheric
Chemistry
and Physics
Discussions

171   agreement, primarily due to uncertainties in instrumental parameters such as

172   inhomogeneities in drift temperature and voltage (Fernández-Maestre et al., 2010). In

173   view of these uncertainties, the instrument standard (the reduced mobility of such a

174   standard is not affected by contaminants in the buffer gas) is needed to provide an

175   accurate constraint on the instrumental parameters, such as voltage, drift length, pressure,

176   and temperature:

177
$$K_0 \times t_d = \frac{L_d^2}{V_d} \frac{P}{1013.25} \frac{273.15}{T} = C_i \qquad (5)$$

178   Tetraethyl ammonium chloride (TEA) is used here as the instrument standard

179   (Fernández-Maestre et al., 2010). Given the well-known K_0 and measured t_d of the

180   protonated TEA ion ($m/z = 130$), Equation (5) yields an instrument constant C_i to

181   calibrate the IMS performance.

182   Unlike TEA, the reduced mobility of species that are more likely to cluster with

183   contaminants can be significantly affected by impurities of the buffer gas. This category

184   of species can be used as a 'mobility standard' to qualitatively indicate the potential

185   contamination in the buffer gas. 2,4-Lutidine, with a well-characterized K_0 value of 1.95

186   cm^2 V^{-1} s^{-1}, is used as such a mobility standard. As shown Figure S4 in the Supplement,

187   the measured mobility of 2,4-Lutidine is 1.5% lower than its theoretical value, indicative

188   of the absence of contaminations in the buffer gas.

189   In the low field limit, the collision cross section of an ion (Ω) with a buffer gas is

190   related to its reduced mobility (K_0) through the modified zero field (so called Mason-

191   Schamp) equation (McDaniel and Mason, 1973; Siems et al., 2012):

192
$$\Omega = \frac{3ze}{16N_0} \left(\frac{2\pi}{k_B \mu T_0}\right)^{1/2} \frac{1}{K_0} \left[1 + \left(\frac{\beta_{MT}}{\alpha_{MT}}\right)^2 \left(\frac{v_d}{v_T}\right)^2\right]^{-1/2} \qquad (6)$$

193   where z is the net number of integer charges on the ion, e is the elementary charge, N_0 is

194   the number density of buffer gas at 273 K and 1013 $mbar$, k_B is the Boltzmann constant,

195   μ is the reduced mass for the molecule-ion pair, T_0 is the standard temperature, v_d is the

196   drift velocity given by Equation (1), v_T is the thermal velocity, and α_{MT} and β_{MT} are

197   correction coefficients for collision frequency and momentum transfer, respectively,

198   given by:

Atmospheric
Chemistry
and Physics
Discussions

Open Access

199
$$\alpha_{MT} = \frac{2}{3}[1 + \hat{m}f_c + \hat{M}f_h] \qquad \beta_{MT} = [\frac{2}{\hat{m}(1+\hat{m})}]^{1/2} \qquad (7)$$

200 where $\hat{m}$ and $\hat{M}$ are mass fractions of the ion and buffer gas molecule, respectively, and f_c

201 and f_h are the fractions of collisions in the cooling and heating classes, respectively. Note

202 that the reduced electric field used in this study is maximized at ~ 2 Td, at which the drift

203 velocity of any given ion is ~ two orders magnitude lower than its thermal velocity, thus

204 the values for f_c and f_h are assigned to be 0.5 and 0.5, respectively. As all measurements

205 in this study were carried out with nitrogen as the buffer gas, the reported collision cross

206 sections will be referred to Ω_{N_2}. Experimental Ω_{N_2} values for a selection of ionic species

207 are consistent with those reported in literatures (see Table S1 in the Supplement).

208

209 **3. Collision Cross Section Modeling**

210 Kinetic theory indicates that the quantity Ω is an orientationally averaged collision

211 integral ($\Omega_{avg}^{(l,l)}$), which depends on the nature of ion-neutral interaction potential

212 (McDaniel and Mason, 1973). Given the potential, the collision integral can be calculated

213 through successive integrations over collision trajectories, impact parameters and energy.

214 Here we adopt two computational methods, i.e., trajectory method and core model, to

215 simulate the average collision integral. The trajectory method is a rigorous calculation of

216 $\Omega_{avg}^{(l,l)}$ by propagating classical trajectories of neutral molecules in a realistic neutral/ion

217 potential consisting of a sum of pairwise Lennard-Jones interactions and ion induced

218 dipole interactions (Mesleh et al., 1996; Shvartsburg and Jarrold, 1996). The core model

219 treats the polyatomic ion as a rigid sphere where the center of charge is displaced from

220 the geometry center. The ion-neutral interaction is approximately represented by the cross

221 section of two rigid spheres during elastic collisions. The (12,4) potential, which includes

222 a long-range polarization term and a short-range repulsion term, is incorporated in the

223 core model (Mason et al., 1972).

224 The two models employed here represent opposite directions in the $\Omega_{avg}^{(l,l)}$ computation

225 methods. The trajectory method is a rigorous calculation of $\Omega_{avg}^{(l,l)}$ in a realistic

226 intermolecular potential yet the computation is time consuming. The core model, on the

Atmospheric
Chemistry
and Physics
Discussions

Open Access

EGU

227   other hand, substantially simplifies the calculation of $\Omega_{avg}^{(l,l)}$ as rigid sphere collisions at the

228   expense of simulation accuracy. We will show shortly that the core model is used for

229   locating individual chemical classes on the 2-D $\Omega_{N_2} - m/z$ space. Within the band

230   developed by each chemical class, molecular structure information can be deduced by

231   comparing the measured collision cross section with those calculated by the trajectory

232   method.

233   3.1 Trajectory Method

234   Molecular structures for L-leucine and D-isoleucine were initially constructed by

235   Avogadro v1.1.1 (Hanwell et al., 2012). For each molecule, both protonation and

236   deprotonation sites are created by placing a positive charge on the N-terminal amino

237   group and a negative charge on the C-terminal carboxyl group, respectively. The

238   geometry of each ion is further optimized using the Hartree-Fock method with the 6-

239   31G(d,p) basis set via GAMESS (Schmidt et al., 1993). Partial atomic charges were

240   estimated using Mulliken population analysis.

241   A freely available software, MOBCAL, developed by Jarrold and coworkers

242   (http://www.indiana.edu/~nano/software.html) was used for computing the collision

243   integrals. The potential term employed in the trajectory method takes the form:

244   $$\Phi(\theta,\phi,\gamma,b,r) = 4\epsilon \sum_i^n [(\frac{\sigma}{r_i})^{12} - (\frac{\sigma}{r_i})^6] - \frac{\alpha_p}{2}(\frac{ze}{n})^2 [(\sum_i^n \frac{x_i}{r_i^3})^2 + (\sum_i^n \frac{y_i}{r_i^3})^2 + (\sum_i^n \frac{z_i}{r_i^3})^2]$$ (8)

245   where θ, ϕ, and γ are three angles that define the geometry of ion-neutral collision, b is

246   the impact parameter, ϵ is the depth of the potential well, σ is the finite distance at which

247   the interaction potential is zero, α_p is the polarizability of the neutral, which is 1.710×10^{-24}

248   cm^3 for N_2 (Olney et al., 1997), n is the number of atoms in the ion, and r_i, x_i, y_i, and z_i

249   are coordinates that define the relative positions of individual atoms with respect to the

250   buffer gas. Values of the Lenard-Jones parameters, ϵ and σ, are taken from the universal

251   force field (Casewit et al., 1992). The ion-quadruple interaction and the orientation of N_2

252   molecule are not considered here (Kim et al., 2008; Campuzano et al., 2012).

253   3.2 Core Model

254   The core model, consisting of a (12-4) central potential displaced from the origin, is

255   used to represent interactions of polyatomic ions with N_2 molecules (Mason et al., 1972).

256   The central potential includes the common long-range r^{-4} polarization energy, as well as

257   the short-range r^{-12} overlap repulsion energy:

258
$$\Phi(r) = \frac{\epsilon}{2} \left\{ \left(\frac{r_m - a}{r - a} \right)^{12} - 3 \left(\frac{r_m - a}{r - a} \right)^{4} \right\} \tag{9}$$

259   where r is the distance between the ion-neutral geometric centers, a is the location of the

260   ionic center of charge measured from the geometrical center of the ion, and r_m is the

261   value of r at the potential minimum. At temperature of 0 K, the *polarization potential* can

262   be expressed as:

263
$$\Phi_{pol}(r) = -\frac{e^2 \alpha_p}{2 r^4} \tag{10}$$

264

265   where α_p is the polarizability of the neutral. Thus ϵ is given by:

266
$$\epsilon = \frac{e^2 \alpha_p}{3 (r_m - a)^4} \tag{11}$$

267   The collision cross section can be expressed in dimensionless form by extracting its

268   dependence on r_m:

269
$$\Omega = \Omega^{(1,1)*} \pi r_m^2 \tag{12}$$

270   Tabulations of the dimensionless collision integral ($\Omega^{(1,1)*}$) can be found in literatures

271   (Mason et al., 1972) as a function of dimensionless temperature (T^*) and core diameter

272   (a^*), given by:

273
$$T^* = \frac{kT}{\epsilon} = \frac{3kT(r_m - a)^4}{e^2 \alpha_p} \qquad a^* = \frac{a}{r_m} \tag{13}$$

274   Polynomial interpolation of the tabulated $\Omega^{(1,1)*}$ yielded an analytical expression of the

275   collision cross section, with r_m and a as adjustable parameters. This expression was then

276   fit to the ion mobility datasets measured in N_2 buffer gas using a nonlinear least-square

Atmospheric
Chemistry
and Physics
Discussions

Open Access

277   regression procedure (Matlab code is available upon request) (Johnson et al., 2004; Kim

278   et al., 2005; Kim et al., 2008). Best-fit parameters, r_m and a, along with predicted vs.

279   measured collision cross section are given in Table S2 in the Supplementary Information.

280

281   **4. Collision Cross Section vs. Mass-to-Charge Ratio 2-D Space**

282   4.1 Distribution of *multi*-Functional Organic Species

283   Figure 1 (A) shows the distribution of organic species, classified as (*di/poly/sugar*)-

284   alcohol, *tertiary*-amine, *quaternary*-ammonium, (*mono/di*)-carbonyl, (*mono/di/tri*)-

285   carboxylic acid, (*di*)-ester, organic sulfate, and *multi*-functional compounds, on the

286   collision cross section vs. mass-to-charge ratio ($\Omega_{N_2} - m/z$) 2-D space. Note that analytes

287   that are detected in different ion modes (+/−) are plotted separately. One feature of the

288   distribution pattern is that species with higher density as pure liquids and carbon

289   oxidation state tend to occupy the lower region of the $\Omega_{N_2} - m/z$ space. This is not

290   surprising given that molecules of smaller collision cross sections tend to be much

291   denser, and potentially more functionalized, than those with extended and open

292   geometries. Furthermore, species of the same chemical class tend to occupy a narrow

293   region and follow a trend line on the $\Omega_{N_2} - m/z$ space. These observations form the basis

294   of potentially utilizing locations and trends on the 2-D space to identify chemical classes

295   to which an unknown compound belongs.

296   Small molecules ($m/z < 200$) with similar size and geometry are situated closely

297   together, as visualized by the 'overlaps' on the space. Improved visual separation of the

298   species within the overlapping region is obtained by transforming Ω_{N_2} to a quantity

299    $\Delta\Omega_{N_2}$, defined as the percentage difference between the measured collision cross section

300   for any given molecular ion and the calculated projection area for a rigid spherical ion-N_2

301   pair with the same molecular mass. A density of 1.2 g cm^{-3}, which represents the average

302   bulk density of ambient organic aerosol (Turpin and Lim, 2001), is used as the reference

303   value. Since this idealized ion-N_2 pair does not account for interaction potentials and

304   molecular conformation, it is only used as a reference state to improve visualization of

305   the $\Omega_{N_2} - m/z$ 2-D space, as shown in Figure 1 (B).

Atmospheric
Chemistry
and Physics
Discussions
Open Access
EGU

306   It is important to note that if these 'overlapping' molecules belong to different

307   chemical classes, they can be resolved based on the fragmentation pattern or

308   characteristic fragments upon collision induced dissociation (CID), as discussed in detail

309   in Section 4.3. Also note that isomeric and isobaric species can be identified by

310   comparing the measured collision cross sections with those obtained from trajectory

311   method simulations, see Section 4.4. As it is highly unlikely that two distinct molecules

312   will produce identical IMS, MS, as well as CID-based MS spectra, the 2-D framework

313   therefore virtually ensures reliable identification of compounds.

314   Reactions involving changes in functionalization and fragmentation can be represented

315   by an intrinsic directionality on the $\Omega_{N_2} - m/z$ space, as illustrated by the distribution

316   pattern of carboxylic acid series shown in Figure 2. Addition of one carbon always leads

317   to an increase in mass and collision cross section, with a generic slope of approximately 5

318    $\text{Å}^2/\text{Th}$. Although the addition of one oxygen in the form of a carbonyl group results in a

319   similar increase in the molecular mass, it leads to a shallower slope compared with that

320   from expanding the carbon chain. Addition of carboxylic or hydroxyl groups leads to a

321   substantial decrease in the collision cross section, due to the formation of a cyclic

322   conformation by the intramolecular hydrogen bonding ($O - H \cdots O^-$).

323   4.2 $\Omega_{N_2} - m/z$ Trend Lines

324   The $\Omega_{N_2} - m/z$ trend line visualized on the 2-D space describes the intrinsic increase

325   in collision cross sections resulting from the increase in molecular mass by extending the

326   carbon backbone or adding functional groups. It has been used for conformation space

327   separation of different classes of biomolecules including lipids, peptides, carbohydrates,

328   and nucleotides (McLean et al., 2005). Here we demonstrate for the first time the

329   presence of trend lines for small molecules of atmospheric interest, and the trend line

330   pattern for each chemical class can be predicted by the core model simulations.

331   Figure 3 shows the measured Ω_{N_2} as a function of mass-to-charge ratio for (A)

332   *tertiary*-amine and *quaternary*-ammonium, (B) (*di/poly/sugar*)-alcohol, and (C)

333   (*mono/oxo/hydroxy*)-carboxylic acid. Also shown are the predicted Ω_{N_2} by the core

334   model, with adjustable parameters optimized by the measured Ω_{N_2} for the subcategory

Atmospheric
Chemistry
and Physics
Discussions

Open Access

335 spanning the largest *m/z* range in each chemical class. Specifically, *quaternary-*

336 ammonium, propylene glycol, and *alkanoic*-acid are used in constraining the core model

337 performance to predict the $\Omega_{N_2} - m/z$ trend lines for amines, alcohols, and carboxylic

338 acids. Species in each chemical class, regardless of the variety in the carbon skeleton

339 structure, occupy a narrow range and appear along a $\Omega_{N_2} - m/z$ trend line. Such a

340 relationship can be further demonstrated by the goodness of the core model predictions,

341 i.e., the difference between predicted and measured Ω_{N_2} for compounds that are not used

342 to optimize the core model performance. For amine series, predicted Ω_{N_2} values for

343 lutidine and pyridine are 8.2% and 0.8% higher, respectively, than the measurements. For

344 alcohol series, the best-fit $\Omega_{N_2} - m/z$ trend line constrained by propylene glycol can be

345 used to predict the distribution of sugars and polyols within 3.5% difference on the space.

346 For carboxylic acid series, hydroxyl-hexadecanoic acid falls closely on the predicted

347 $\Omega_{N_2} - m/z$ trend line, despite the presence of an alcohol group on the C_{16} carbon chain.

348 Predicted Ω_{N_2} values for *oxo*-carboxylic acids are 4.4% – 6.1% lower than the

349 observations. Benzoic acid exhibits a relatively large measurement-prediction gap (6.7%)

350 potentially due to the presence of an aromatic ring.

351 Overall, the demonstrated $\Omega_{N_2} - m/z$ trend lines for carboxylic acids, amines, and

352 alcohols provide a useful tool for classification of structurally related compounds on the

353 space. It is worth noting that the core model optimization and simulation can be certainly

354 extended to other functionalities with the availability of chemical standards. Mapping out

355 the locations and distribution patterns for various functionalities on the 2-D space would

356 greatly facilitate structural identification of unknown compounds of atmospheric interest.

357 4.3 Molecular Structure Elucidation of *multi*-Functional Species

358 The demonstrated $\Omega_{N_2} - m/z$ relationship provides a useful tool to identify the

359 chemical class to which an unknown species belongs. To further identify its molecular

360 structure, knowledge on the electrospray ionization mechanism for the generation of

361 *quasi*-molecular ions, as well as fragmentation patterns of the molecular ion upon

362 collision induced dissociation (CID), is required.

Atmospheric
Chemistry
and Physics
Discussions

363   For species investigated in this study, the positive mass spectra collected for amines

364   and amino acids show major ions at m/z values corresponding to the protonated cations

365   ([M+H]$^+$). Sodiated clusters ([M+Na]$^+$) of esters were observed as the dominant peak in

366   the ESI(+) spectra. Aromatic aldehydes combine with a methyl group ([M+CH$_3$]$^+$) via the

367   gas-phase aldol reaction between protonated aldehydes and methanol in the positive

368   mode. Sugars and polyols can be readily ionized in both positive and negative mode with

369   the addition of a proton or sodium ion or deprotonation. Extensive formation of

370   oligomers is observed from the positive mass spectra of propylene glycol, with the

371   deprotonated propanol (–OCH$_2$CH(CH$_3$)–) as the primary building block. Monoanions

372   ([M-H]$^-$) were exclusively observed in the negative mass spectra of (*mono/di/tri/multi*)-

373   carboxylic acids due to the facile ionization afforded by the carboxylic group. An

374   exhibition of molecular formulas of ionic species is given in Table 1.

375   The instrument used in this study enables the collision induced dissociation of the

376   abovementioned precursor ions after ion mobility separation but prior to the mass

377   spectrometer (IMS-CID-MS). As a consequence, product ions exhibit the identical

378   mobility (drift time) with that of the precursor ion. IMS-CID-MS spectra for individual

379   compounds are then generated by the extraction of "mobility-selected" MS spectra that

380   contain both precursor and fragments. The major advantage of this approach is that it is

381   possible to obtain fragmentation spectra for all precursor ions simultaneously. This is in

382   contrast to MS/MS techniques which require the isolation of a small mass window prior

383   to fragmentation which can be a problem for very complex samples or time-resolved

384   analysis. Figure 4 shows the measured drift time for the precursor and product ions

385   generated from species representative of amines, aldehydes, carboxylic acids, esters, and

386   nitro compounds. Collision induced dissociation patterns of these species are used to

387   elucidate the fragmentation mechanisms for corresponding functional groups. The

388   deprotonated carboxylic acid is known to undergo facile decarboxylation to produce a

389   carbanion. If additional carboxylic groups are present in the molecule, combined loss of

390   water and carbon dioxide is expected (Grossert et al., 2005). Alternatively, the presence

391   of an –OH group adjacent to the carboxylic group would usually result in a neutral loss of

392   formic acid (Greene et al., 2013), see the fragmentation pattern for 16-

393   hydroxyhexadecanoic acid as an illustration. Scission of the C–O bond in the ester

Atmospheric
Chemistry
and Physics
Discussions

Open Access

394 structure or the C–O bond between the secondary/tertiary carbon and the alcoholic

395 oxygen is observed for the ester series examined, consistent with previous studies (Zhang

396 et al., 2015). A primary fragmentation resulting in loss of CO was evident in the spectrum

397 of methylate derivative of protonated carbonyls ($RCHOCH_3^+$) (Neta et al., 2014). The

398 IMS-CID-MS spectrum of deprotonated 4-nitrophenol is shown as a representative of

399 organic nitro compounds. Two dominant peaks at m/z 108 and m/z 92 are observed,

400 resulting from the neutral loss of NO and NO_2, respectively.

401 Signal intensities of the fragments from the CID pathway of the precursor ion depend

402 on the collision voltage, as shown in Figure 5. At low collision voltages, the precursor

403 ions predominate with transmission optimized at approximately 5 V potential gradient.

404 As the collision voltage increases, the intensity of the precursor ion decreases and that of

405 each product ion increases, eventually reaching a maximum level, and then decreases due

406 to subsequent fragmentation. The dependence of the product ion abundance on the

407 collision voltage provides information on the relative strength of the covalent bond at

408 which the parent molecule fragments. Consequently, the energy required to induce a

409 certain fragmentation pathway could potentially also serve as an additional parameter for

410 structure elucidation. For example, the predominance of the product ion at m/z 149

411 suggests that cleavage of the O-O bond in the ester moiety is the dominant fragmentation

412 pathway upon CID of dioctyl phthalate ($C_{24}H_{38}O_4$).

413

414 4.4 Resolving Isomeric Mixtures

415 Here we demonstrate the separation and identification of isomers on the $\Omega_{N_2} - m/z$

416 space using the mixture of L-leucine and D-isoleucine as an illustration. Leucine can be

417 directly ionized by electrospray in both positive and negative modes due to the presence

418 of amino and carboxyl groups. Figure 6 (A and B) shows a single peak that corresponds

419 to the protonated ($[M+H]^+$, $m/z = 132$) and deprotonated ($[M–H]^-$, $m/z = 130$) forms of

420 the leucine mixture, respectively, in the positive and negative MS spectra. Upon further

421 separation based on their distinct mobility in the N_2 buffer gas, the leucine mixture is

422 clearly resolved in the positive mode, while a broad peak is observed in the negative ion

423 mobility spectrum, see Figure 6 (C and D). Note that a typical IMS resolving power

Atmospheric
Chemistry
and Physics
Discussions

Open Access

424   (t/dt_{50}) of 100 leads to a baseline separation of leucine isomers that differ by 0.3 ms in the

425   measured drift time. Figure 6 (E-H) shows the IMS spectra for individual leucine

426   isomeric configurations, which provide precise constraints for the peak assignment in the

427   leucine mixture. Also given here are the measured vs. predicted collision cross sections

428   for each isomer, with predictions lower by 3.3 ~ 6.9% compared with the measurements.

429   However, despite the underprediction, the model using trajectory method correctly

430   predicts the relative collision cross sections of the isomers and therefore also the order in

431   which they appear in the IMS spectrum. The underprediction of Ω_{N_2} may result from the

432   simplification that linear N_2 molecules are considered as elastic and specular spheres in

433   the current model configuration (Larriba-Andaluz and Hogan Jr, 2014). Further

434   development of the model to more appropriately predict Ω_{N_2} values is needed.

435

436   **5. Conclusions**

437   We propose a new metric, collision cross section (Ω), for characterizing organic

438   species of atmospheric interest. Collision cross section represents an effective interaction

439   area between a charged molecule and neutral buffer gas as it travels through under the

440   action of a weak electric field, and thus relates to the chemical structure and 3-D

441   conformation of this molecule. The collision cross section of individual molecular ions is

442   calculated from the ion mobility measurements using an Ion Mobility Spectrometer. In

443   this study, we provide the derived Ω_{N_2} values for a series of organic species including

444   amines, alcohols, carbonyls, carboxylic acids, esters, organic sulfates, and *multi-*

445   *functional* compounds.

446   The collision cross section, when coupled with mass-to-charge ratio, provides a 2-D

447   framework for characterizing the molecular signature of atmospheric organic aerosol.

448   The $\Omega_{N_2} - m/z$ space is employed to guide our fundamental understanding of processes

449   of organic aerosol formation and evolution in the atmosphere. We show that different

450   chemical classes tend to develop unique narrow bands with trend lines on the $\Omega_{N_2} - m/z$

451   space. Trajectories associated with atmospheric transformation mechanisms either cross

452   or follow these trend lines through the space. The demonstrated $\Omega_{N_2} - m/z$ trend lines

Atmospheric
Chemistry
and Physics
Discussions

453   provide a useful tool for resolving various functionalities in the complex OA mixture.

454   These intrinsic trend lines can be predicted by the core model, which provides a guide for

455   locating unknown functionalities on the $\Omega_{N_2} - m/z$ space.

456   Within each band that that belongs to a particular chemical class on the space, species

457   can be further separated based on their distinct structures and geometries. We

458   demonstrate the utility of collision induced dissociation technique, upon which the

459   resulted product ions share the identical drift time as the precursor ion, to facilitate the

460   elucidation of molecular structures of OA constituents. We employ the $\Omega_{N_2} - m/z$

461   framework for separation of isomeric mixtures as well by comparing the measured

462   collision cross sections with those predicted using the trajectory method. Further

463   advances in algorithms to correctly predict collision cross sections *ab initio* from

464   molecular coordinates are therefore also expected to significantly improve identification

465   of unknowns.

466

473

474   **Appendix:**

475   a (Å): the location of the ionic center of charge from the geometrical center of the ion.

476   a^*: the dimensionless core diameter.

477   α_{MT}: the correction coefficient for collision frequency.

478   α_p (cm^3): the polarizability of the neutral.

479   β_{MT}: the correction coefficient for momentum transfer.

480   C_i: the instrument constant that is used to calibrate the IMS performance.

481   ϵ (eV): the depth of the potential well.

482   E_d (V/cm): the electric field intensity in the drift tube.

483   Φ (eV): the ion-neutral interaction potential.

484   f_c: the fraction of collisions in the cooling classes.

485   f_h: the fraction of collisions in the heating classes.

486   k_B (m^2 kg s^{-2} K^{-1}): Boltzmann constant.

487   K (cm^2 V^{-1} s^{-1}): the characteristic mobility constant of a given ion.

488   K_0 (cm^2 V^{-1} s^{-1}): the reduced mobility constant of a given ion.

489   L_d (V/cm): the length of the drift tube.

490      $\hat{m}$: the mass fraction of the ion in the ion-molecule pair.

491      $\hat{M}$: the mass fraction of the buffer gas molecule (N$_2$) in the ion-molecule pair.

492   m/z (Th): the mass-to-charge ratio of any given ion.

493   N_0 (# cm^{-3}): the number density of buffer gas at 273 K and 1013 $mbar$.

494   Ω (Å^2): the collision cross section.

495   Ω_{N_2} (Å^2): the collision cross section using N$_2$ as the buffer gas.

496      $\Omega_{avg}^{(l,l)}$: the orientationally averaged collision integral.

497      $\Omega^{(l,l)*}$: the dimensionless collision integral.

498   P ($mbar$): the pressure in the drift region.

499   r (Å): the distance between the ion-neutral geometric centers.

500   r_m (Å): the value of r at the potential minimum.

501   σ (Å): the finite distance at which the interaction potential is zero.

502   T (K): the buffer gas temperature.

503   T_0 (K): the standard temperature.

504   T^*: the dimensionless temperature.

505   t_a (s): the recorded arrival time of the ion clouds at the detector.

506   t_d (s): the time of ion clouds spent in the drift tube.

507   t_0 (s): the transport time of ion clouds from the exit of the drift tube to the MS detector.

508   v_d (s): the average velocity of an ion in the drift tube.

509   v_T (m s^{-1}): the thermal velocity.

510   V_d (V): the voltage applied to the drift tube.

511   z: the net number of integer charges on the ion.

Atmospheric
Chemistry
and Physics
Discussions

512 **References:**

513 Campuzano, I., Bush, M. F., Robinson, C. V., Beaumont, C., Richardson, K., Kim, H.,
514 and Kim, H. I.: Structural characterization of drug-like compounds by ion mobility mass
515 spectrometry: comparison of theoretical and experimentally derived nitrogen collision
516 cross sections, Anal. Chem., 84, 1026-1033, 2012.

517 Casewit, C. J., Colwell, K. S., and Rappe, A. K.: Application of a universal force field to
518 organic molecules, J. Am. Chem. Soc., 114, 10035-10046, 1992.

519 Donahue, N. M., Kroll, J. H., Pandis, S. N., and Robinson, A. L.: A two-dimensional
520 volatility basis set–Part 2: Diagnostics of organic-aerosol evolution, Atmos. Chem. Phys.,
521 12, 615-634, 2012.

522 Dwivedi, P., Wu, P., Klopsch, S. J., Puzon, G. J., Xun, L., and Hill Jr, H. H.: Metabolic
523 profiling by ion mobility mass spectrometry (IMMS), Metabolomics, 4, 63-80, 2008.

524 Eiceman, G. A., and Stone, J. A.: Ion mobility spectrometers in national defence, Anal.
525 Chem., 76, 390-397, 2004.

526 Eiceman, G. A., Karpas, Z., and Hill Jr, H. H.: Ion mobility spectrometry, CRC press,
527 2013.

528 Ewing, R. G., Atkinson, D. A., Eiceman, G. A., and Ewing, G. J.: A critical review of ion
529 mobility spectrometry for the detection of explosives and explosive related compounds,
530 Talanta, 54, 515-529, 2001.

531 Fernandez-Maestre, R., Harden, C. S., Ewing, R. G., Crawford, C. L., and Hill, H. H., Jr.:
532 Chemical standards in ion mobility spectrometry, Analyst, 135, 1433-1442, 2010.

533 Greene, L. E., Grossert, J. S., and White, R. L.: Correlations of ion structure with
534 multiple fragmentation pathways arising from collision-induced dissociations of selected
535 a-hydroxycarboxylic acid anions, J. Mass Spectrom., 48, 312-320, 2013.

536 Groessl, M., Graf, S., and Knochenmuss, R.: High resolution ion mobility-mass
537 spectrometry for separation and identification of isomeric lipids, Analyst, 140, 6904-
538 6911, 2015.

539 Grossert, J. S., Fancy, P. D., and White, R. L.: Fragmentation pathways of negative ions
540 produced by electrospray ionization of acyclic dicarboxylic acids and derivatives, Can. J.
541 Chem., 83, 1878-1890, 2005.

542 Hallquist, M., Wenger, J. C., Baltensperger, U., Rudich, Y., Simpson, D., Claeys, M.,
543 Dommen, J., Donahue, N. M., George, C., Goldstein, A. H., Hamilton, J. F., Herrmann,
544 H., Hoffmann, T., Iinuma, Y., Jang, M., Jenkin, M. E., Jimenez, J. L., Kiendler-Scharr,
545 A., Maenhaut, W., McFiggans, G., Mentel, T. F., Monod, A., Prévôt, A. S. H., Seinfeld,
546 J. H., Surratt, J. D., Szmigielski, R., and Wildt, J.: The formation, properties and impact
547 of secondary organic aerosol: current and emerging issues, Atmos. Chem. Phys., 9, 5155-
548 5236, 10.5194/acp-9-5155-2009, 2009.

549 Hanwell, M. D., Curtis, D. E., Lonie, D. C., Vandermeersch, T., Zurek, E., and
550 Hutchison, G. R.: Avogadro: An advanced semantic chemical editor, visualization, and
551 analysis platform, J. Cheminform., 4, 10.1186/1758-2946-4-17, 2012.

Atmospheric
Chemistry
and Physics
Discussions

Open Access

552   Heald, C. L., Kroll, J. H., Jimenez, J. L., Docherty, K. S., DeCarlo, P. F., Aiken, A. C.,
553   Chen, Q., Martin, S. T., Farmer, D. K., and Artaxo, P.: A simplified description of the
554   evolution of organic aerosol composition in the atmosphere, Geophys. Res. Lett., 37,
555   L08803, 10.1029/2010GL042737, 2010.

556   Johnson, P. V., Kim, H. I., Beegle, L. W., and Kanik, I.: Electrospray ionization ion
557   mobility spectrometry of amino acids: ion mobilities and a mass-mobility correlation, J.
558   Phys. Chem. A, 108, 5785-5792, 2004.

559   Kanu, A. B., Dwivedi, P., Tam, M., Matz, L., and Hill, H. H.: Ion mobility–mass
560   spectrometry, J. Mass Spectrom., 43, 1-22, 2008.

561   Kaplan, K., Graf, S., Tanner, C., Gonin, M., Fuhrer, K., Knochenmuss, R., Dwivedi, P.,
562   and Hill Jr, H. H.: Resistive Glass IM-TOFMS, Anal. Chem., 82, 9336-9343, 2010.

563   Kim, H., Kim, H. I., Johnson, P. V., Beegle, L. W., Beauchamp, J. L., Goddard, W. A.,
564   and Kanik, I.: Experimental and theoretical investigation into the correlation between
565   mass and ion mobility for choline and other ammonium cations in N2, Anal. Chem., 80,
566   1928-1936, 2008.

567   Kim, H. I., Johnson, P. V., Beegle, L. W., Beauchamp, J. L., and Kanik, I.: Electrospray
568   ionization ion mobility spectrometry of carboxylate anions: Ion mobilities and a mass-
569   mobility correlation, J. Phys. Chem. A, 109, 7888-7895, 2005.

570   Krechmer, J. E., Groessl, M., Zhang, X., Junninen, H., Massoli, P., Lambe, A. T.,
571   Kimmel, J. R., Cubison, M. J., Graf, S., Lin, Y. H., Budisulistiorini, S. H., Zhang, H.,
572   Surratt, J. D., Knochenmuss, R., Jayne, J. T., Worsnop, D. R., Jimenez, J. L., and
573   Canagaratna, M. R.: Ion Mobility Spectrometry-Mass Spectrometry (IMS-MS) for on-
574   and off-line analysis of atmospheric gas and aerosol species, Atmos. Meas. Tech.
575   Discuss., 2016, 1-34, 10.5194/amt-2016-132, 2016.

576   Kroll, J. H., Donahue, N. M., Jimenez, J. L., Kessler, S. H., Canagaratna, M. R., Wilson,
577   K. R., Altieri, K. E., Mazzoleni, L. R., Wozniak, A. S., Bluhm, H., Mysak, E. R., Smith,
578   J. D., Kolb, C. E., and Worsnop, D. R.: Carbon oxidation state as a metric for describing
579   the chemistry of atmospheric organic aerosol, Nature Chem., 3, 133-139, 2011.

580   Larriba-Andaluz, C., and Hogan Jr, C. J.: Collision cross section calculations for
581   polyatomic ions considering rotating diatomic/linear gas molecules, J. Chem. Phys., 141,
582   194107, doi.org/10.1063/1.4901890, 2014.

583   Liu, X., Valentine, S. J., Plasencia, M. D., Trimpin, S., Naylor, S., and Clemmer, D. E.:
584   Mapping the human plasma proteome by SCX-LC-IMS-MS, J. Am. Soc. Mass
585   Spectrom., 18, 1249-1264, 2007.

586   Mason, E. A., O'Hara, H., and Smith, F. J.: Mobilities of polyatomic ions in gases: core
587   model, J. Phys. B, 5, 169-172, 1972.

588   McDaniel, E. W., and Mason, E. A.: The mobility and diffusion of ions in gases, Wiley,
589   1973.

590   McLean, J. A., Ruotolo, B. T., Gillig, K. J., and Russell, D. H.: Ion mobility–mass
591   spectrometry: a new paradigm for proteomics, Int. J. Mass Spectrom., 240, 301-315,
592   2005.

593   Mesleh, M. F., Hunter, J. M., Shvartsburg, A. A., Schatz, G. C., and Jarrold, M. F.:
594   Structural information from ion mobility measurements: effects of the long-range
595   potential, J. Phys. Chem., 100, 16082-16086, 1996.

596   Neta, P., Simón‐Manso, Y., Liang, Y., and Stein, S. E.: Loss of H2 and CO from
597   protonated aldehydes in electrospray ionization mass spectrometry, Rapid Commun.
598   Mass Spectrom., 28, 1871-1882, 2014.

599   Olney, T. N., Cann, N. M., Cooper, G., and Brion, C. E.: Absolute scale determination
600   for photoabsorption spectra and the calculation of molecular properties using dipole sum-
601   rules, Chem. Phys., 223, 59-98, 1997.

602   Roscioli, K. M., Zhang, X., Li, S. X., Goetz, G. H., Cheng, G., Zhang, Z., Siems, W. F.,
603   and Hill, H. H.: Real time pharmaceutical reaction monitoring by electrospray ion
604   mobility-mass spectrometry, Int. J. Mass Spectrom., 336, 27-36, 2013.

605   Schmidt, M. W., Baldridge, K. K., Boatz, J. A., Elbert, S. T., Gordon, M. S., Jensen, J.
606   H., Koseki, S., Matsunaga, N., Nguyen, K. A., and Su, S.: General atomic and molecular
607   electronic structure system, J. Comput. Chem., 14, 1347-1363, 1993.

608   Shvartsburg, A. A., and Jarrold, M. F.: An exact hard-spheres scattering model for the
609   mobilities of polyatomic ions, Chem. Phys. Lett., 261, 86-91, 1996.

610   Shvartsburg, A. A., Liu, B., Jarrold, M. F., and Ho, K.-M.: Modeling ionic mobilities by
611   scattering on electronic density isosurfaces: Application to silicon cluster anions, J.
612   Chem. Phys., 112, 4517-4526, 2000.

613   Siems, W. F., Viehland, L. A., and Hill Jr, H. H.: Improved momentum-transfer theory
614   for ion mobility. 1. Derivation of the fundamental equation, Anal. Chem., 84, 9782-9791,
615   2012.

616   Turpin, B. J., and Lim, H.-J.: Species contributions to PM2.5 mass concentrations:
617   Revisiting common assumptions for estimating organic mass, Aerosol Sci. Tech., 35,
618   602-610, 2001.

619   Zhang, X., and Seinfeld, J. H.: A functional group oxidation model (FGOM) for SOA
620   formation and aging, Atmos. Chem. Phys., 13, 5907-5926, 2013.

621   Zhang, X., Knochenmuss, R., Siems, W. F., Liu, W., Graf, S., and Hill, H. H., Jr.:
622   Evaluation of Hadamard transform atmospheric pressure ion mobility time-of-flight mass
623   spectrometry for complex mixture analysis, Anal. Chem., 86, 1661-1670, 2014.

624   Zhang, X., McVay, R. C., Huang, D. D., Dalleska, N. F., Aumont, B., Flagan, R. C., and
625   Seinfeld, J. H.: Formation and evolution of molecular products in α-pinene secondary
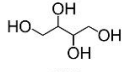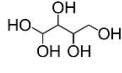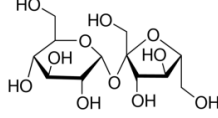626   organic aerosol, Proc. Natl. Acad. Sci. USA, 112, 14168-14173, 2015.

627

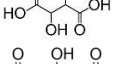Atmospheric
Chemistry
and Physics
Discussions

Open Access
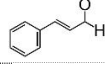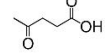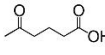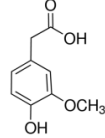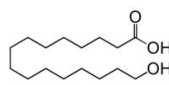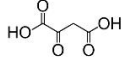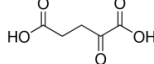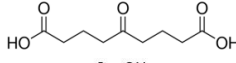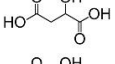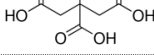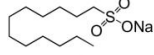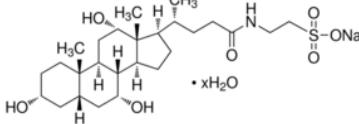
Table 1. Overview of organic standards investigated in this study.

Class	Chemical	Molecular Formula	Ion		Ω_{N_2} (Å^2)	Molecular Structure
			Formula	m/z		
Amine	Tetraethyl ammonium chloride	C$_8$H$_{20}$NCl	[M-Cl]$^+$	130.16	122.1	
	Tetrapropyl ammonium chloride	C$_{12}$H$_{28}$NCl	[M-Cl]$^+$	186.10	143.8	
	Tetrabutyl ammonium iodide	C$_{16}$H$_{36}$NI	[M-I]$^+$	242.17	165.8	
	Tetrapentyl ammonium chloride	C$_{20}$H$_{44}$NCl	[M-Cl]$^+$	298.35	190.0	
	Tetraheptyl ammonium chloride	C$_{28}$H$_{60}$NCl	[M-Cl]$^+$	410.47	236.5	
	2,4-Lutidine	C$_7$H$_9$N	[M+H]$^+$	108.08	123.4	
	2,6-Di-tert-butylpyridine	C$_{13}$H$_{21}$N	[M+H]$^+$	192.17	145.0	
Amino acid	L-Leucine	C$_6$H$_{13}$NO$_2$	[M+H]$^+$	132.10	137.8	
			[M–H]$^-$	130.09	144.4	
	D-Isoleucine	C$_6$H$_{13}$NO$_2$	[M+H]$^+$	132.10	135.2	
			[M–H]$^-$	130.09	140.3	
mono Carboxylic Acid	Benzoic acid	C$_7$H$_6$O$_2$	[M–H]$^-$	121.03	128.6	
	Octanoic acid	C$_8$H$_{16}$O$_2$	[M–H]$^-$	143.11	144.7	
	2-Butyloctanoic acid	C$_{12}$H$_{24}$O$_2$	[M–H]$^-$	199.17	162.0	
	Tridecanoic acid	C$_{13}$H$_{26}$O$_2$	[M–H]$^-$	213.19	166.2	CH$_3$(CH$_2$)$_{10}$CH$_2$
	Pentadecanoic acid	C$_{15}$H$_{30}$O$_2$	[M–H]$^-$	241.22	173.7	CH$_3$(CH$_2$)$_{12}$CH$_2$
	Palmitic acid	C$_{16}$H$_{32}$O$_2$	[M–H]$^-$	255.23	177.9	CH$_3$(CH$_2$)$_{13}$CH$_2$
	Stearic acid	C$_{18}$H$_{36}$O$_2$	[M–H]$^-$	283.26	185.4	CH$_3$(CH$_2$)$_{15}$CH$_2$
	Oleic acid	C$_{18}$H$_{34}$O$_2$	[M–H]$^-$	281.25	186.9	CH$_3$(CH$_2$)$_6$CH$_2$

Atmospheric
Chemistry
and Physics
Discussions

	Succinic acid	$C_4H_6O_4$	$[M–H]^-$	117.02	124.6	
	Glutaric acid	$C_5H_8O_4$	$[M–H]^-$	131.03	128.4	
	Adipic acid	$C_6H_{10}O_4$	$[M–H]^-$	145.05	131.5	
	Pimelic acid	$C_7H_{12}O_4$	$[M–H]^-$	159.06	134.0	
di/multi Carboxylic Acid	Azelaic acid	$C_9H_{16}O_4$	$[M–H]^-$	187.09	143.5	
	Sebacic acid	$C_{10}H_{18}O_4$	$[M–H]^-$	201.11	148.9	
	1,2,3-Propane tricarboxylic acid	$C_6H_8O_6$	$[M–H]^-$	175.02	122.2	
	Cyclohexane tricarboxylic acid	$C_9H_{12}O_6$	$[M–H]^-$	215.06	135.0	
	Mellitic acid	$C_{12}H_6O_{12}$	$[M–H_2O–H]^-$	322.96	154.6	
	Dibutyl oxalate	$C_{10}H_{18}O_4$	$[M+Na]^+$	225.11	170.0	
Ester	Dibutyl phtahlate	$C_{16}H_{22}O_4$	$[M+Na]^+$ $[2M+Na]^+$	301.14 579.29	192.4 255.5	
	Dioctyl phthalate	$C_{24}H_{38}O_4$	$[M+H]^+$	391.28	203.6	
Alcohol	Propylene glycol	$C_3H_8O_2$	$[2M-2H_2O+Na]^+$	215.12	144.8	
			$[4M-3H_2O+Na]^+$	273.17	156.4	
			$[5M-4H_2O+H]^+$	309.23	165.7	
			$[5M-4H_2O+Na]^+$	331.21	169.6	
			$[6M-5H_2O+H]^+$	367.27	179.1	
			$[6M-5H_2O+Na]^+$	389.24	181.6	
			$[7M-6H_2O+H]^+$	425.31	190.8	
			$[7M-6H_2O+Na]^+$	447.28	193.9	
			$[8M-7H_2O+H]^+$	483.35	204.7	
			$[8M-7H_2O+Na]^+$	505.32	206.2	
			$[9M-8H_2O+H]^+$	541.39	218.5	
			$[9M-8H_2O+Na]^+$	563.36	219.3	
			$[10M-9H_2O+H]^+$	599.42	231.3	
			$[10M-9H_2O+Na]^+$	621.40	231.8	

	DL-Threitol	$C_4H_{10}O_4$	[M+Na]$^+$	145.05	133.0	
	Xylitol	$C_5H_{12}O_5$	[M–H]$^-$	151.06	131.2	
	Sucrose	$C_{12}H_{22}O_{11}$	[M–H]$^-$ [M+Na]$^+$	341.11 365.11	167.6 175.1	
Carbonyl	Hexane-3,4-dione	$C_6H_{10}O_2$	[M+H]$^+$ [M+CH$_3$]$^+$	115.08 129.09	115.7 121.3	
	Acetophone	C_8H_8O	[M+CH$_3$]$^+$	135.08	120.4	
	Cinnamaldehyde	C_9H_8O	[M+CH$_3$]$^+$	147.08	123.9	
multi Functional Compound	Levulinic acid	$C_5H_8O_3$	[M–H]$^-$	115.04	130.0	
	4-Acetylbutyric acid	$C_6H_{10}O_3$	[M–H]$^-$	129.06	134.5	
	Homovanillic acid	$C_9H_{10}O_4$	[M–H]$^-$	181.05	147.7	
	16-Hydroxy hexadecanoic acid	$C_{16}H_{32}O_3$	[M–H]$^-$	271.22	183.7	
	Oxaloacetic acid	$C_4H_4O_5$	[M–H]$^-$	131.06	118.3	
	Ketoglutaric acid	$C_5H_6O_5$	[M–H]$^-$	145.01	120.9	
	Oxoazelaic acid	$C_9H_{14}O_5$	[M–H]$^-$	201.08	133.3	
	Malic acid	$C_4H_6O_5$	[M–H]$^-$	133.01	111.4	
	Tartaric acid	$C_4H_6O_6$	[M–H]$^-$	149.01	116.0	
	Citric acid	$C_6H_8O_7$	[M–H]$^-$	191.02	123.0	
Organic Sulfate	Sodium Dodecyl sulfate	$C_{12}H_{25}SO_4Na$	[M–Na]$^-$	265.15	163.6	
	Sodium Taurocholate	$C_{26}H_{44}SO_7NNa$	[M–Na]$^-$	514.28	206.4	

Atmospheric
Chemistry
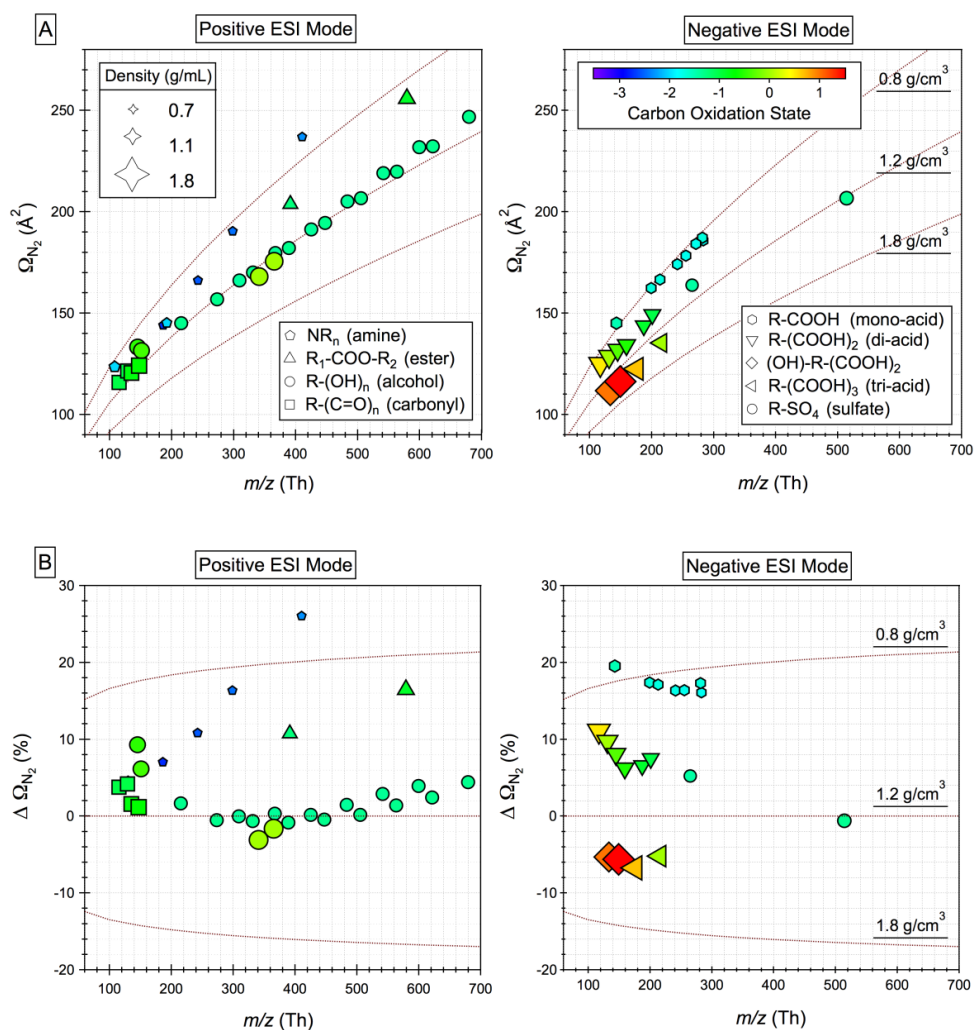and Physics

Discussions

Open Access

Figure 1. Distribution of organic species including alcohol (R-(OH)$_n$, n = 2-8), amine (NR$_3$), *quaternary*-ammonium (NR$_4$), carbonyl (R-(C=O)$_n$, n = 1-2), carboxylic acid (R-(COOH)$_n$, n = 1-3), ester (R$_1$-COO-R$_2$), organic sulfate (R-SO$_4$), and *multi*-functional compounds ((OH)-R-(COOH)$_2$) on the (A) $\Omega_{N_2} - m/z$ space and (B) $\Delta\Omega_{N_2} - m/z$ space.
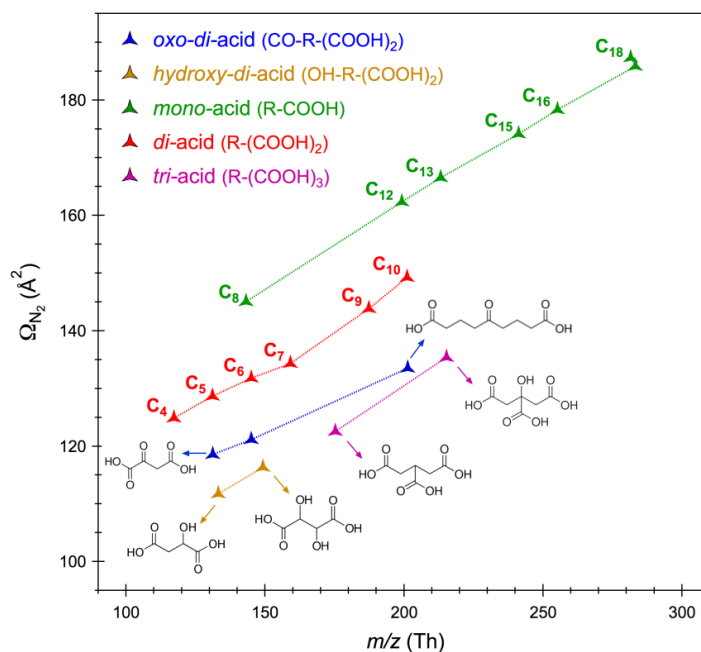
Figure 2. Trajectories associated with reactions involving functionalization (changes in the type and number of functional groups) and fragmentation (changes in the carbon chain length) through the 2-D $\Omega_{N_2} - m/z$ space using carboxylic acid series as an illustration.
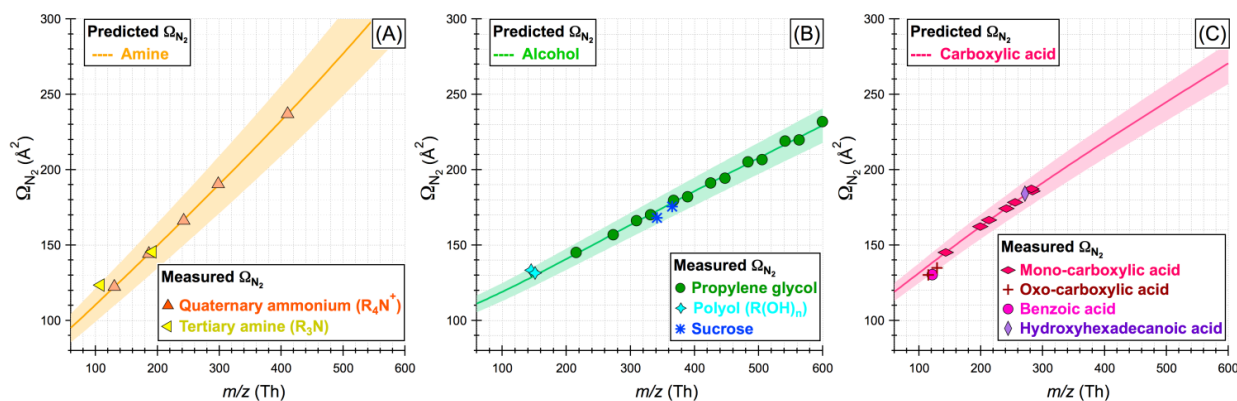
Figure 3. Measured collision cross sections (Ω_{N_2}) for (A) *tertiary*-amine and *quaternary*-ammonium, (B) (*di/poly/sugar*)-alcohol, and (C) (*mono/oxo/hydroxy*)-carboxylic acid as a function of the mass-to-charge ratio. Also shown are the predicted $\Omega_{N_2} - m/z$ trend lines for amine, alcohol, and carboxylic acid by the core model. Here, *quaternary*-ammonium, propylene glycol, and C_8-C_{18} *alkanoic*-acid are used to optimize the adjustable parameters in the core model (The markers are in the same color as the trend lines). The colored shade in each figure represents the maximum deviations (8.21%, 3.54%, and 6.69% for amine, alcohol, and carboxylic acid, respectively) of the predicted Ω_{N_2} from the measured Ω_{N_2} for species that are not used to constrain the core model. A single plot showing the separation of these three chemical classes is given in Figure S5 in the supplement.

Atmospheric
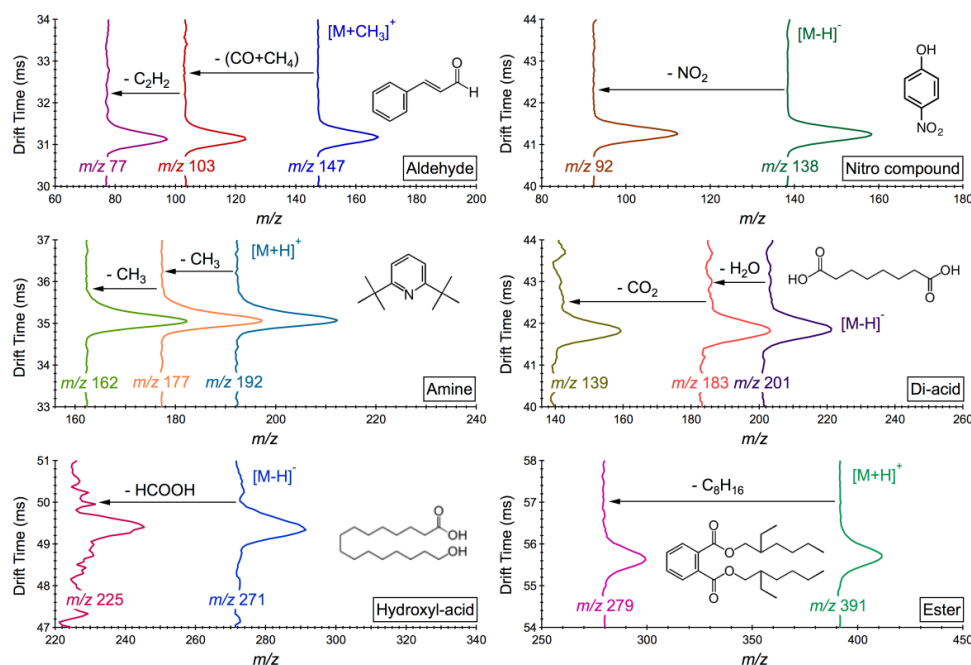Chemistry
and Physics
Discussions

Figure 4. Collision induced dissociation patterns for molecular ions generated from cinnamaldehyde, dioctyl phthalate, 2,6-di-tert-butylpyridine, 4-nitrophenol, 16-hydroxyhexadecanoic acid, and sebacic acid on the mobility – mass framework with mass-to-charge ratio on the *x*-axis and drift time on the *y*-axis. The corresponding mobility selected MS spectra for each species is given in Figure S6 in the supplement.

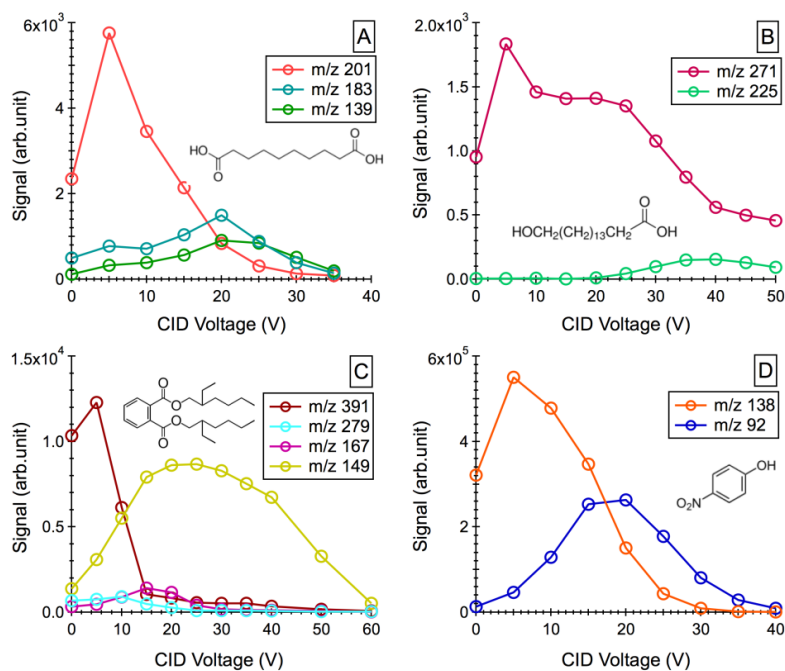Atmospheric
Chemistry
and Physics
Discussions

Open Access

Figure 5. Product ion peak intensities as a function of collision voltage in the 'mobility-selected' MS spectra of (A) deprotonated sebacic acid, (B) deprotonated 16-hydroxyhexadecanoic acid, (C) sodiated dioctyl phthalate, and (D) deprotonated 4-nitrophenol.
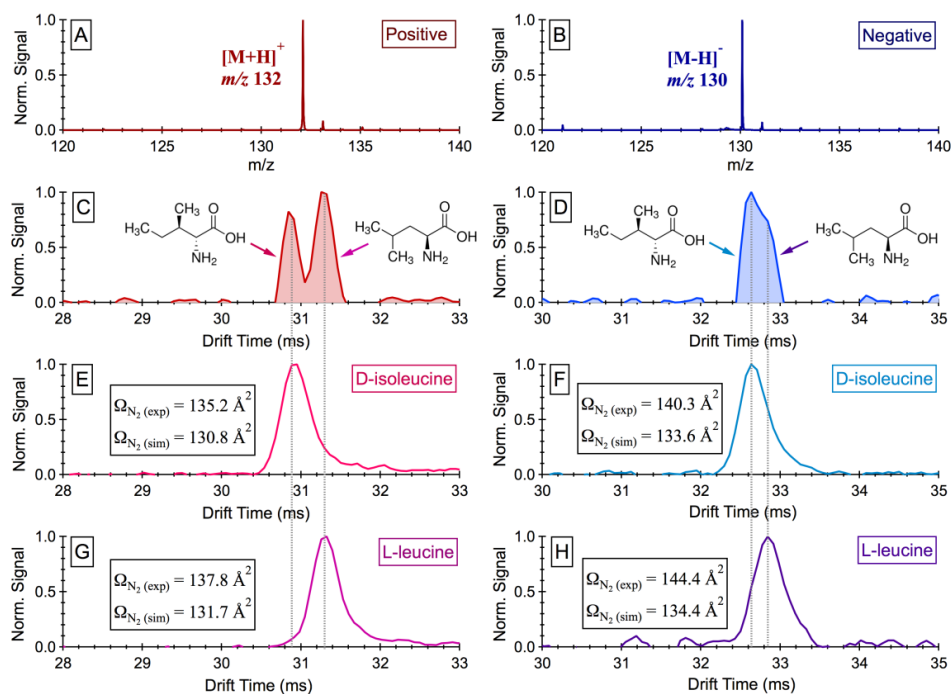
Atmospheric
Chemistry
and Physics
Discussions

Figure 6. (A/B) ESI mass spectra collected for an equi-molar mixture (20 μM each) of L-leucine and D-isoleucine in positive and negative mode. (C/D) Measured drift time distributions for the leucine mixture in positive and negative mode. (E/F) Measured vs. predicted Ω_{N_2} for D-isoleucine, together with its drift time distributions in positive and negative mode. (G/H) Measured vs. predicted Ω_{N_2} for L-leucine, together with its drift time distributions in positive and negative mode. Note that all measurements were performed at ~ 303 K and ~ 1019 mbar with an electric field strength of 414 and 403 V cm^{-1} in the positive and negative mode, respectively.